sustainability

MDPI

Article

Fractal Characterization of Brass Corrosion in Cavitation Field in Seawater

Alina Bărbulescu [1,*] and Cristian Ștefan Dumitriu [2,*]

[1] Department of Civil Engineering, Transilvania University of Brașov, 5, Turnului Street, 900152 Brașov, Romania
[2] Faculty of Mechanical Engineering and Robotics in Constructions, Technical University of Civil Engineering of Bucharest, 122, Lacul Tei Av., 020396 Bucharest, Romania
* Correspondence: alina.barbulescu@unitbv.ro (A.B.); cris.dum.stef@gmail.com (C.Ș.D.)

Abstract: Cavitation is a physical process that produces complex effects on the machines and components working in conditions where it acts. One effect is the materials-mass loss by corrosion–erosion when components are introduced into fluids under cavitation. The analysis of the damages produced by cavitation is generally performed by using different destructive and non-destructive experimental techniques. Most studies on materials' behavior in cavitation refer to the erosion–corrosion mechanism, and very few investigate the fissure propagation by fractal methods. None have investigated the fractal characteristics of the sample surface after erosion–corrosion or the multifractal characteristics of materials' mass variation in time in a cavitation field. Therefore, this research proposes a computational approach to determine the pattern of materials' damages produced by ultrasound cavitation. The studied material is a brass, introduced in seawater. Fractal and multifractal techniques are applied to the series of the absolute mass loss per surface and the sample's micrography after corrosion. Such an approach has not been utilized for such a material in similar experimental conditions. This study emphasizes that the box dimension of the series of the absolute mass loss per surface is close to one, and its behaviour is close to a non-/monofractal. It is demonstrated that the material's surface corrosion is not uniform, and its multifractal character is highlighted by the $f(\alpha)-$ spectrum and the multifractal dimensions, which have the following values: the capacity dimension = 1.5969, the information dimension = 1.49836, and the correlation dimension = 1.4670.

Keywords: erosion–corrosion; cavitation; ultrasound; fractal dimension; multifractal

Citation: Bărbulescu, A.; Dumitriu, C.Ș. Fractal Characterization of Brass Corrosion in Cavitation Field in Seawater. *Sustainability* **2023**, *15*, 3816. https://doi.org/10.3390/su15043816

Academic Editors: Marijana Hadzima-Nyarko and Dorin Radu

Received: 31 December 2022
Revised: 6 February 2023
Accepted: 16 February 2023
Published: 20 February 2023

1. Introduction

An ultrasound signal passing through a liquid produces the cyclic apparition, increase, and collapse of the vapor bubbles formed in the liquid. This phenomenon is called cavitation [1]. It is accompanied by discontinuities in the liquid's state (as a result of the pressure decrease under critical limits) [2] and high temperatures at the time of the bubbles' collapse. Other consequences of cavitation are vibrations, noise, sonoluminescence, emulsification, unpassivation, corrosion of the materials immersed in the liquid, and the apparition of an electrical signal at the boundary of the cavitation region [3–6].

Copper alloys are used in different industries, such as in naval engineering for building propellers, ballast installation, and bilge systems. Given their industrial applications, different scientists [7–11] have analyzed the behavior of such alloys under cavitation. Schüssler and Exner [7], Wharton and Stokes [9], and Wharton et al. [10] studied the corrosion of bronzes with Ni and Al in seawater, aiming to explain the corrosion mechanism and the unpassivation effect. The same kind of alloys attracted the interest of Basumatary and Wood [11], who presented their experimental results on Ni-Al bronze in a NaCl solution (3.5%). The behavior of some materials for ship propellers has been investigated by Basumatary et al. [10], who found a better resistance of the bronze sample to corrosion–erosion produced by cavitation compared with that of the stainless steel in their experiment.

Some mechanical properties' variations of Cu alloys after the corrosion in different solutions of electrolytes with concentrations between 0 and 0.71 M were studied by Hamidah et al. [12]. Alfantazi et al. [13] investigated the influence of the pH variation (from 6.5 to 10) on the potentiodynamic polarization behavior (in 1 M NaCl solution) of Cu–30Ni, Cu-30Zn, and 90Cu–8Al–2Fe alloys.

The most used investigation methods in this type of research are open circuit potential (OCP) [14,15], electrochemical impedance spectroscopy (EIS) [14], electrochemical noise measurement [16], and synergy tests [10]. These methods show that the resistance of some copper alloys to cavitation in seawater increases when Sn is added to bronze [17]. Furthermore, adding Ni to their composition improves the mechanical characteristics of the bronzes with Al and Fe in a cavitation field.

Apart from the corrosion mechanism and the variation of the metallic materials' mechanical properties, another research direction has been to model the variation of the Cu alloys in the cavitation field in various liquids [7,18–20].

Introduced by Mandelbrot [21], the fractal theory has been developed and applied to assess the time series characteristics in many scientific fields, such as hydrometeorology [22,23], geology [24], signal analysis [25], and remote sensing [26]. The fractal study of images is a valuable tool in the medical sciences for correct diagnostics, such as for pulmonary diseases [27,28], dental imaging [29,30], and trabecular bone investigations [31]. Moreover, fractal analysis has become a tool to determine materials' structures' behavior during the working and failure periods. The fractal applications to corrosion and cracking problems can be classified into (a) the experimental study of fractal characteristics of sections (in materials) and the determination of the fractal measures [32], (b) establishing the correlations between the materials' mechanical properties and their fractal dimensions [33,34], and (c) detecting the physical mechanism of fractal fracture [35,36].

Zavdoveev et al. [37] studied the variation of the fractal dimension of different metals in the severe plastic deformation process. The variation of the fractal dimension of the crack propagation in Ni-Cr steel in two heat treatments was analyzed by Dlouhý and Strnadel [38]. The characterization of some concrete surfaces cracking and their correlation with the corrosion of the steel bars that reinforce the concrete was reported by Ji et al. [36], Li et al. [39], and Xu et al. [40].

The roughness of different steel surfaces was investigated by Davis and Hall [41] and Karolczak et al. [42]. Their studies can be successfully applied to surfaces' corrosion evaluation. Kim and Hwang [43] proposed the evaluation of a fractal technique for corrosion studies. They used the Hust parameter to analyze the electrochemical noise collected during the corrosion of two types of steel in a NaCl solution.

Songbo et al. [44] investigated the critical pit's fractal character in relation to corroded steel's degradation. Zhang et al. [45] studied the surfaces of corroded thin steel plates. The corrosion inhibition of steel in a bromide solution was investigated using the rescaled range analysis (introduced by Hurst), which belongs to the fractal techniques [46].

Despite various studies using the fractal methodology for corrosion analysis, only a few scientists [47,48] have studied the corrosion of copper alloys by fractal methodology, none of which focused on the ultrasound cavitation field. In the presented context, this article proposes a computational approach to determine the pattern of the damages of a brass sample subject to the ultrasound cavitation produced in seawater using fractal and multifractal techniques. The fractal dimensions of the series of absolute mass loss variation per surface and of the image of the corroded sample's surface are estimated. The results complete the findings from [18,19,49], which proposed different mathematical models for the mass loss and mass loss per surface of some copper alloys in the cavitation field in similar conditions. The main advantage of this methodology is that it provides a non-destructive evaluation of corrosion using the fractal dimensions of the corrosion surface [50].

2. Materials and Methods

2.1. Materials

The experimental plant built for studying the corrosion–erosion in ultrasound cavitation is presented in Figure 1.

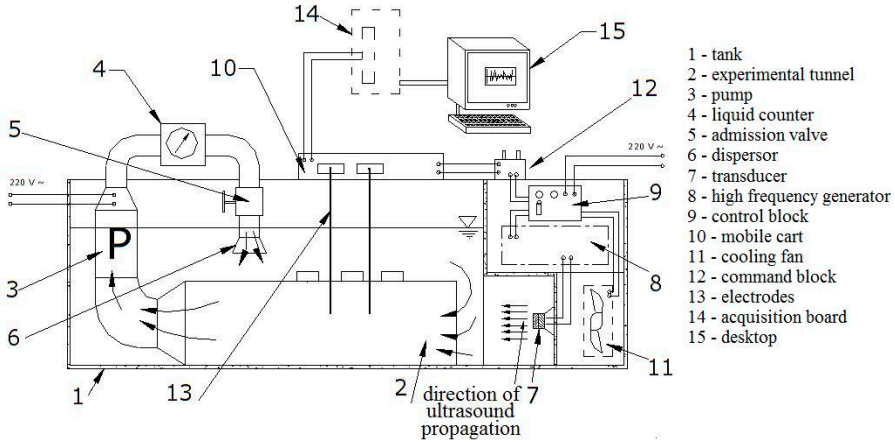

Figure 1. Setup for the cavitation study [5].

The principal components are [5,6]:

- The reservoir (1) for the liquid;
- The generator (8) that produces the ultrasounds, working at 220 V, 18 kHz, and 80, 120, or 180 W;
- The piezoceramic transducer (7) that enters into oscillation as a response to the high-frequency signal received from the generator, producing the cavitation;
- The control panel (9) used to select the ultrasound generator's working regimen;
- The cooler (11) utilized for keeping constant the liquid's temperature;
- The measurement electrodes employed for capturing the signal induced by cavitation in the experiments designed for this aim;
- The acquisition data unit (14), which collects the electrical signal produced by the ultrasound cavitation;
- The pump (3), which is switched on for experiments in the circulating liquid medium.

The following conditions were met in the experiments whose results are presented here. The material samples were immersed in seawater (with pH = 7, the concentration of sodium chloride = 22.17 g/L, sulfate ion = 0.31 g/L, Fe (and Ni) 0.051 (and 0.0033) mg/L, and total hardness = 6.27 meq/L) in the cavitation field for 1320 min. Every 20 min, they were extracted, cleaned, and weighed. The water temperature was maintained at 20 °C. The studied material was brass with 2.75% Pb and 38.45% Zn besides Cu (57.95 %).

The time series of the absolute mass loss (computed as the difference between the initial sample mass and its mass at the measurement moment) per surface was built from the collected data. The corrosion effect on the material was observed using a scanning electron microscope (SEM, JSM-6360, JEOL, Tokyo, Japan).

Finally, the fractal and multifractal analyses of the absolute mass loss curve and the corroded surface were performed, as described in the next section.

2.2. Methodology

"Fractal" is a word derived from "fractus," a Latin adjective meaning "fragmented" or "irregular." A characteristic of the fractals is their length or area dependence on the measurement scale [26]. Fractal objects also have a self-similarity property (the scale invariance of the object shape), which does not hold exactly for objects found in nature.

Therefore, the dimension of such a set, called fractal dimension, d, is empirically estimated by the Formula (1), as for the self-similar mathematical sets:

$$d = \frac{\ln(n_\varepsilon)}{\ln(1/\varepsilon)}, \quad (1)$$

where n_ε is the number of the set's parts and ε is the scale ratio [21].

The most used method to evaluate fractal dimension is *box counting*. It relies on covering the figure with a quadratic grid whose cell edge length increases at each step of the algorithm. The counted cells are those containing at least one point. The dimension computed by this procedure is called the *box dimension* (d_{box}).

Generally, the procedure of empirical evaluation of d_{box} is the following:

- Set different sizes of the sides and determine the "cells" necessary to cover the object,
- Fit the least squares linear regression of the measured cells vs. the sizes of the sides in a log-log scale,
- Determine d_{box} as the slope of the line from the previous step.

In this study, the box dimension was estimated by increasing the dimensions of the boxes that covered the curve from two pixels to the maximum possible size, using an arithmetic progression with a ratio equal to two and a grid rotation of 12°.

To obtain the *correlation dimension* (d_{corr}), windows (circular or square) were built around the points of the analyzed figure, and the average number of points contained by the windows was counted. The procedure was repeated for different values of the sizes (from the smallest to the highest ones) [51].

The *capacity dimension* (d_{cap}) is defined by:

$$d_{cap} = -\lim_{\substack{\varepsilon \to 0 \\ \varepsilon > 0}} \frac{\ln(N_\varepsilon)}{\ln(\varepsilon)}, \quad (2)$$

(when this limit is defined), $\varepsilon > 0$ and N_ε being the element's size and the number of elements (of a certain size) covering the set, respectively [52].

The *information dimension* (d_{inf}) is estimated by [53]:

$$d_{inf} = \lim_{\substack{\varepsilon \to 0 \\ \varepsilon > 0}} \frac{\sum_{i=1}^{N_\varepsilon} P_i(\varepsilon) \ln(P_i(\varepsilon))}{\ln(\varepsilon)}, \quad (3)$$

where ε is the element's size and $P_i(\varepsilon)$ is the normalized probability that the i^{th} cell is not empty.

From a practical viewpoint, the set whose dimension should be evaluated is covered with boxes for computing d_{inf}. If the size of the box edge is ε, $P_i(\varepsilon)$ is the ratio between the number of points in the i^{th} box and the total number of points. The numerator, *information entropy* ($I(\varepsilon)$), is computed first. The slope of the regression line of $I(\varepsilon)$ vs. $\ln(\varepsilon)$ approximates d_{inf}.

It can be proved [53] that the following inequalities are true:

$$d_{corr} \leq d_{inf} \leq d_{cap}. \quad (4)$$

The reader may see [54,55] for details on these dimensions.

There are different methods utilized to assess multifractality. One of them involves the computation of the singularity spectrum of a certain measure used to estimate the differences between the pixels of the analyzed images. In our study, it needed to distinguish

the corroded parts from the non-altered ones. For this aim, giving a 2-dim field covered by a grid, a measure function is defined by:

$$P_{jk}(\varepsilon) = n_{jk} / \sum n_{jk} \quad (5)$$

where n_{jk} and $P_{jk}(\varepsilon)$ are the percentage of the grey value and the probability of its apparition, in the (*j*,*k*) box with an ε size, respectively. Therefore, the probability of the apparition of some pixels in a certain box depends on the box size to an exponent that is variable when covering the image. Thus, a *partition function* is constructed by:

$$Z_q(\varepsilon) = \sum P_{jk}^q(\varepsilon) = \varepsilon^{\tau(q)}, \quad (6)$$

where $q \in \mathbf{R}$ is the moment's order.

In the case of the multifractal character, $\tau(q)$, called the *mass exponent*, can be estimated by fitting a least squares linear curve of $\lg(Z_q(\varepsilon))$ vs. $\lg(\varepsilon)$ [56]. It can also be computed by:

$$\tau_q = \lim_{\varepsilon \to 0} \frac{\lg(\sum P_{jk}^q(\varepsilon)}{\lg(\varepsilon)}. \quad (7)$$

In the case of a monofractal field, the chart of τ_q versus q is a straight line for all values of q.

Another way to characterize the multifractal sets is by using a Legendre transform to define the *f(α)- spectrum function* (or *singularity spectrum),* by

$$f(\alpha(q)) = q\alpha(q) - \tau(q) = q\frac{d\tau(q)}{dq} - \tau(q), \quad (8)$$

where α is *the singularity* (*Hölder*) *exponent* [55,57].

Plotting *f(α)* against α gets the *multifractal spectrum*.
The multifractality strength can be evaluated by the singularity spectrum amplitude $\Delta\alpha = \alpha_{\max} - \alpha_{\min}$. The multifractality's strength increases with $\Delta\alpha$.

Renyi [58] introduced D_q, *Renyi's dimension* (or *generalized dimension*), as a multifractality measure, by:

$$D_q = \frac{1}{q-1} \lim_{\varepsilon \to 0} \frac{\lg(\sum Z_q(\varepsilon))}{\lg(\varepsilon)}, \quad (9)$$

where ε is the box size. The relationship between D_q and τ_q is [58]:

$$\tau_q = (q-1)D_q. \quad (10)$$

In the multifractality case, the graph of the curve obtained by plotting D_q vs. q had a reverse sigmoid shape, whereas, in the monofractal situation, the shape of the curve was linear (tending to be horizontal).

To perform this analysis, the software utilized was FracLac for ImageJ 4.5.2. (Charles Sturt University, Australia/Canada) [59].

3. Results and Discussion

3.1. Analysis of the Absolute Mass Loss Per Surface Curve

The absolute mass loss of the sample per surface is presented in Figure 2.

According to [49], the trend of mass loss (Δm_t) per surface (S) can be described by the equation:

$$\Delta m_t / S = 0.0732 + 0.1922t + 0.0008t^2, \quad (11)$$

where t is the time and the determination coefficient is $R^2 = 0.9957$. A good evaluation of the trend of the mass loss per surface is also given by the linear model, with $R^2 = 0.9951$:

$$\Delta m_t / S = 0.0138 + 0.2105t. \quad (12)$$

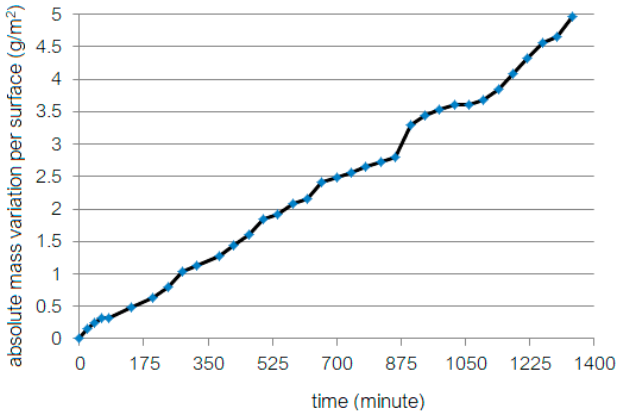

Figure 2. The absolute mass loss of the sample per surface.

The fractal analysis was performed in the first stage. It included the box dimension estimation, as presented in Figure 3. In Figure 3a, the average number of boxes (Avg Count) used to cover the curve in the experiment is plotted against the box size (ε). The chart has an exponentially decreasing shape. The same dependence was represented in an ln-ln scale to determine the box dimension, resulting in the chart from Figure 3b. The slope of the least squares regression line through the points of coordinates (ε, lnε) is the box-counting dimension.

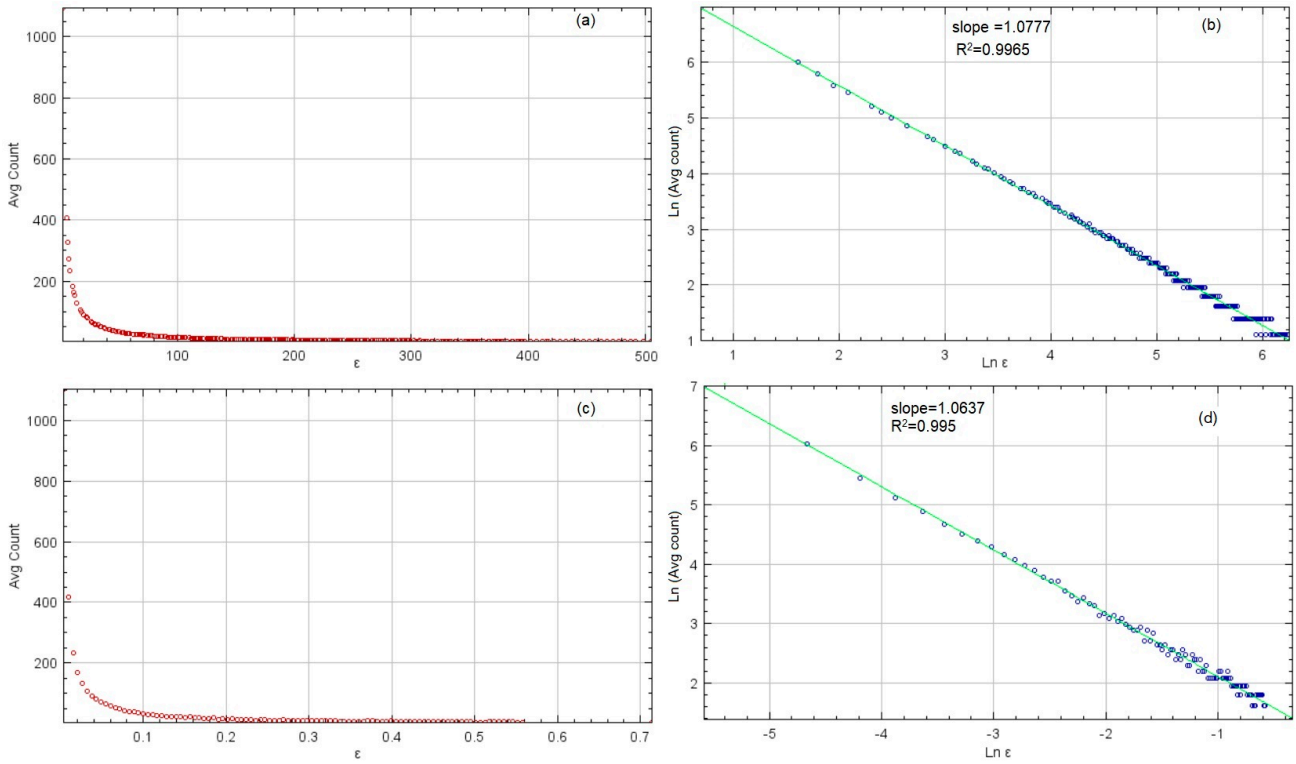

Figure 3. (**a**) The average number of boxes (Avg Count) vs. the box size (ε). (**b**) Regression line showing the box dimension of the curve from Figure 2. (**c**) Plot of the average number of boxes for the cover with the highest R^2. (**d**) Regression line showing the box dimension estimation using the cover with the lowest box dimension. The charts are processed from the output of FracLac.

Since experiments were performed by rotating the boxes that cover the curve from Figure 2 by multiples of 15°, different values of the box dimensions were obtained. Figure 3c,d show the same results as in Figure 3a,b, but for the experiments with the lowest box dimensions among all the experiments.

In all experiments (30–given that the rotation angle was set to 15°) the d_{box} varied between 1.0637 and 1.0889, with R^2 above 0.995, and the standard deviation (SD) under 0.0368. Taking into account the ln(average count) (denoted in Figure 3 by Ln(Avg Count)), $d_{box} = 1.0777$, with $R^2 = 0.9965$, and SD = 0.0115. Therefore, 1.0777 can be considered a good estimation of the box dimension. Moreover, d_{box} is close to one, which is in concordance with the remark that a linear equation describes the mass loss trend (so, the series exhibits a nonfractal/monofractal behavior).

Figure 4 displays the chart of the mass exponent, τ_q, computed for the curve in Figure 2. The chart shows a straight line, indicating a monofractal behavior of the series of mass loss per surface. The slope of the line is 1.0895, close to the value of the box dimension.

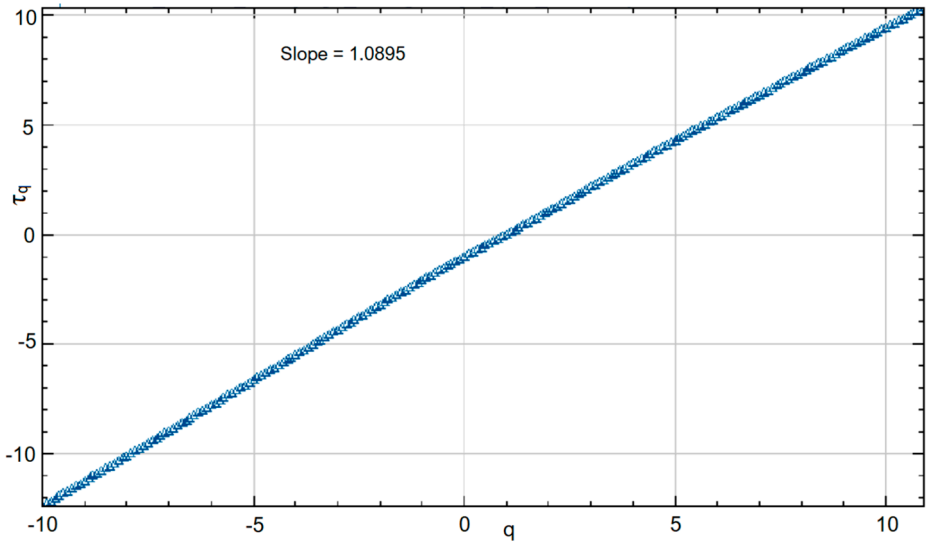

Figure 4. The chart of the mass exponent, τ_q.

To determine the multifractal character of the series, Renyi's dimension was computed, and the shape of the D_q chart vs. q was observed. Conclusions were drawn based on the knowledge that a sigmoidal S-shape on the chart is to be expected in a multifractal case. Figure 5 presents the plot of D_q as a function of q, for $q \in [-10, 10]$. The chart of D_q vs. q shows a straight line, indicating that D_q is a constant, equal to $D_0 = 1.22$. Therefore, this remark led to the same conclusion of the multifractality absence, already drawn from the analysis of Figure 4.

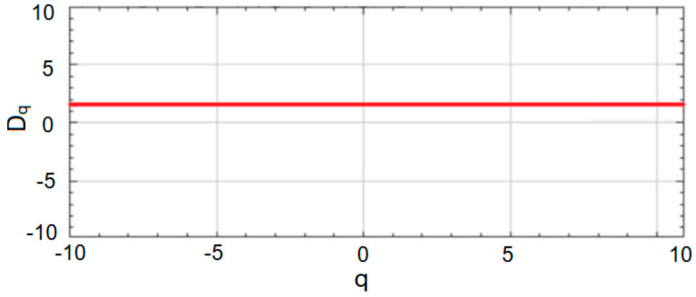

Figure 5. The dimension spectrum D_q.

Figure 6a,b contain the chart of the $f(\alpha)$–spectrum in two experiments. Figure 6c shows the $f(\alpha)$–spectrum for the average values in all the experiments. The maximum

$f(\alpha)$ value in Figure 6c is 1.0546, for α = 1.0751. In half of the performed experiments, the $f(\alpha)$–spectrum indicated a non-/monofractal behavior ($f(\alpha)$ converges). In the other half, a multifractal behavior was indicated, but the $\Delta\alpha$ values were very small, suggesting a low multifractality intensity. Therefore, in the absence of concordance in all the experimental results, the series multifractality must be rejected. By combining these findings with those drawn from the charts of τ_q, and D_q, one may conclude that the analyzed time series does not present the multifractality property.

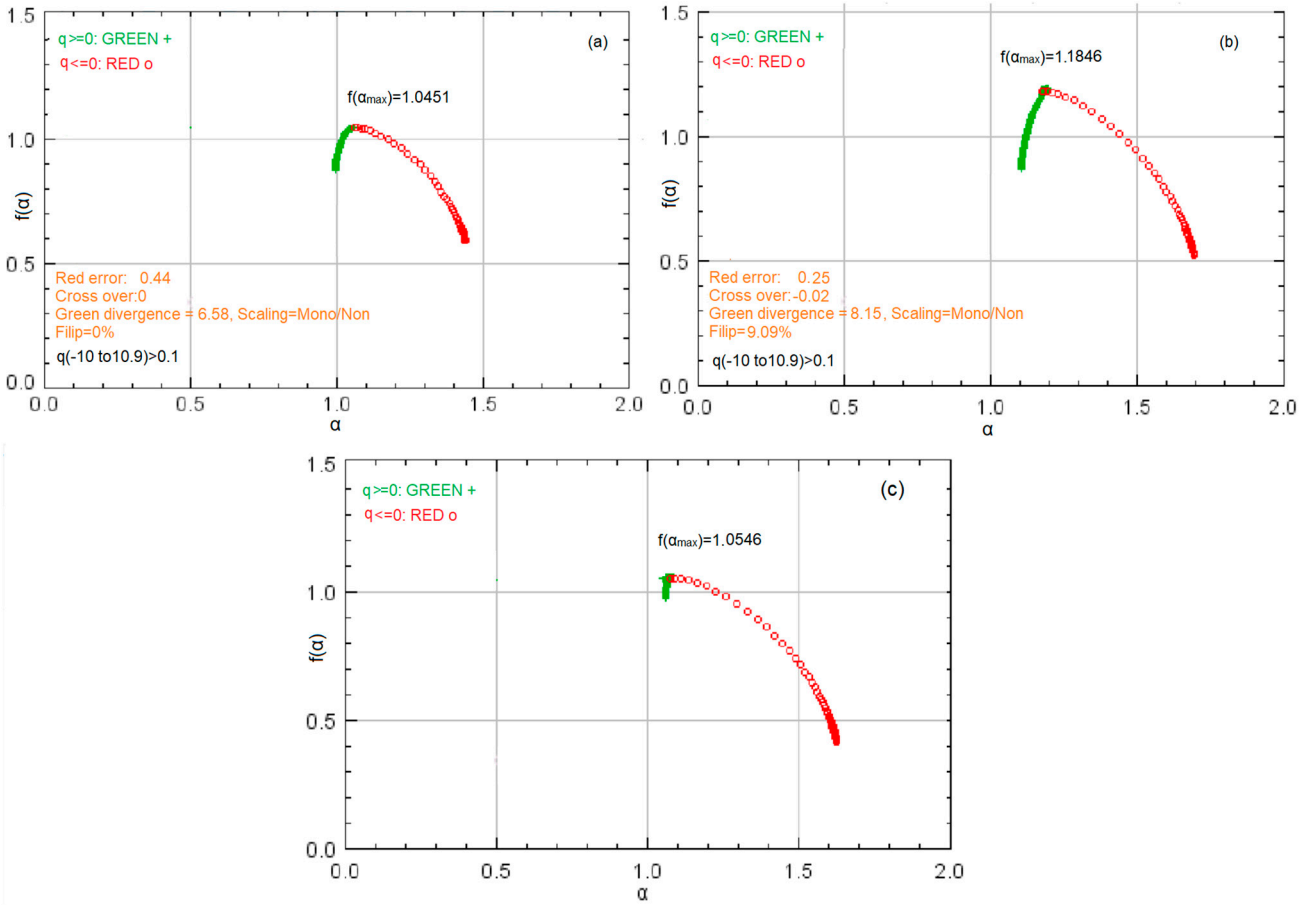

Figure 6. The $f(\alpha)-$ spectrum in two experiments with (**a**) a flip of 0% and (**b**) a flip of 9.09%. (**c**) The $f(\alpha)-$ spectrum computed by averaging the results of all the experiments.

3.2. Fractal Analysis of the Sample Surface after Corrosion

Figure 7 shows the corrosion morphology before (Figure 7a) and after (Figure 7b) the experiment, for comparison purposes. The black dots from Figure 7a, found in Figure 7b as well, indicate the material's compounds. The black zones from Figure 7b represent the corroded regions, while the white ones are those not affected by corrosion–erosion.

Before running the experiments for detecting the fractal/multifractal property of the sample's surface after the ultrasound action, the sample's picture was binarized using ImageJ, with the default setting. Figure 7b indicates the presence of a certain pattern and some shapes' irregularities and orientations. Only a few local corrosion points are isolated (characteristics of pitting), most of them being connected. The morphology becomes more complex when the corrosion processes advance, at the same time as the mass loss augmentation. This observation is in concordance with the findings of Xu et al. [40] for other metallic materials.

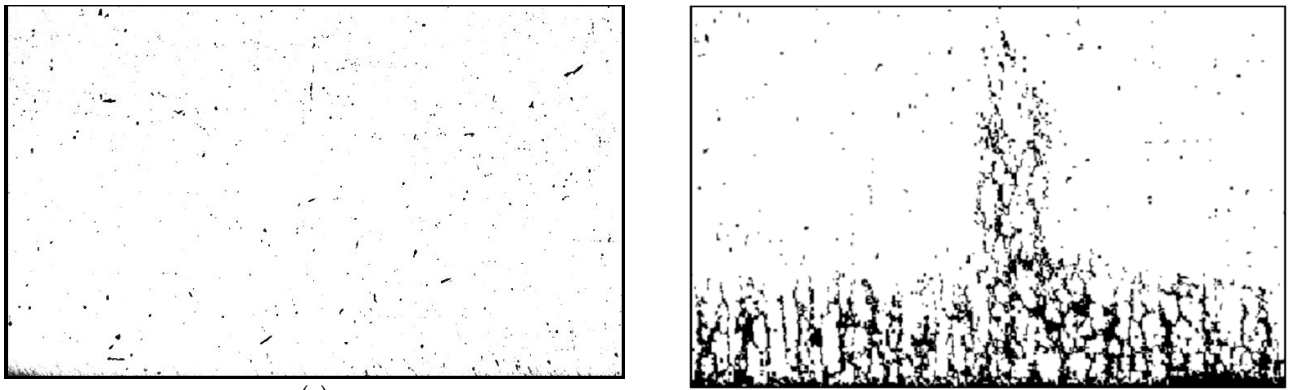

(**a**) (**b**)

Figure 7. (**a**) Image of the sample's surface before the corrosion–erosion. (**b**) Image of the sample's surface after the corrosion–erosion in the seawater of the β′ phase in the surface layer of the sample, with a magnification of 180.

Figure 8a contains the plot of the logarithm of the number of occupied boxes used to cover the image (Ln(count)) vs. the logarithm of the box side length (Ln(ε)) and the regression line fitted to determine the box dimension of the corroded part of the sample from Figure 7b.

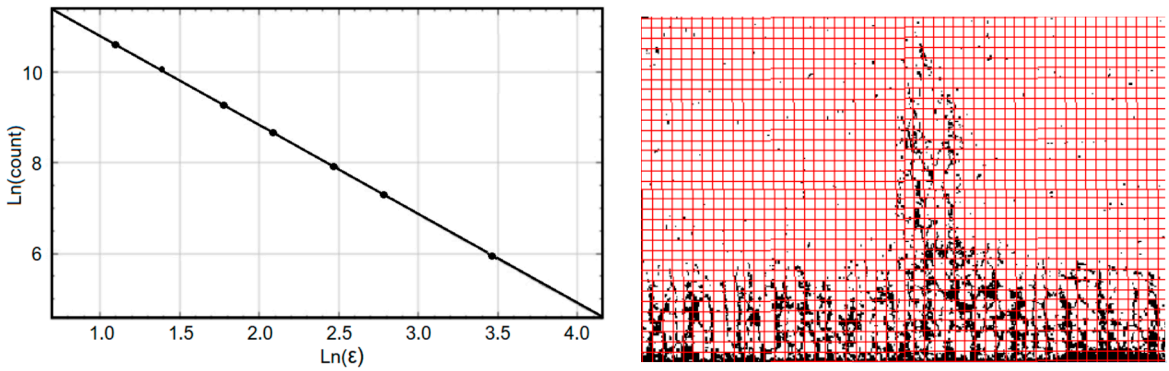

(**a**) (**b**)

Figure 8. The computation of the box dimension of the image from Figure 7b: (**a**) The least squares regression line drawn to determine the box dimension. (**b**) Grid covering the image of the corroded sample, used in the box dimension computation.

The dots in Figure 8a (the experimental values) are aligned along the regression line, indicating a very good fit of the least squares regression line whose slope is the box dimension. Figure 8b shows a cover of the binary image by a red grid, used during the computation procedure of the box dimension. The settings for running the algorithm were similar to those from the experiments related to the sample mass loss on the surface. With these settings, the box dimension varied in the interval [1.5257, 1.6689], with an average $d_{box} = 1.5692$, and a standard deviation of 0.0269. R^2 was above 0.989 in all cases, indicating the estimation accuracy.

Figure 9 presents the chart of the τ_q exponent against q, for $q \in [-10, 10.9]$.

The existence of at least two segments with different slopes is noticed in this chart. For $q \in [-10, 0.6]$, the slope of the least square regression line of τ_q as a function of q is 2.1792 (with $R^2 = 1$). For $q \in [0.6,\ 2.0]$, the slope of the regression line is 1.6714 ($R^2 = 0.9987$), and for $q \in [\ 2.1,\ 10.9]$, it is 1.4064 ($R^2 = 0.9999$). Such a chart emphasizes the multifractal character of the analyzed image. To confirm this finding, the dimension spectrum was determined in each experiment and as an average of all experiments.

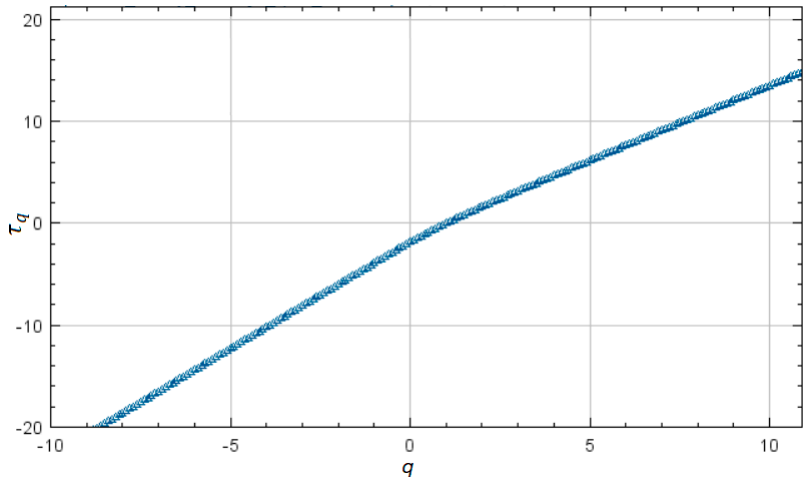

Figure 9. The chart of the mass exponent, τ_q .

Figure 10 depicts the average D_q spectrum. The shape is inverse-sigmoidal, as expected in the multifractal case. Therefore, the capacity, information, and correlation dimensions were computed to characterize the multifractality degree. They correspond to particular values of $q = 0$, 1, and 2, respectively: $d_{cap} = D_0 = 1.5969$, $d_{inf} = D_1 = 1.49836$, and $d_{cor} = D_2 = 1.4670$.

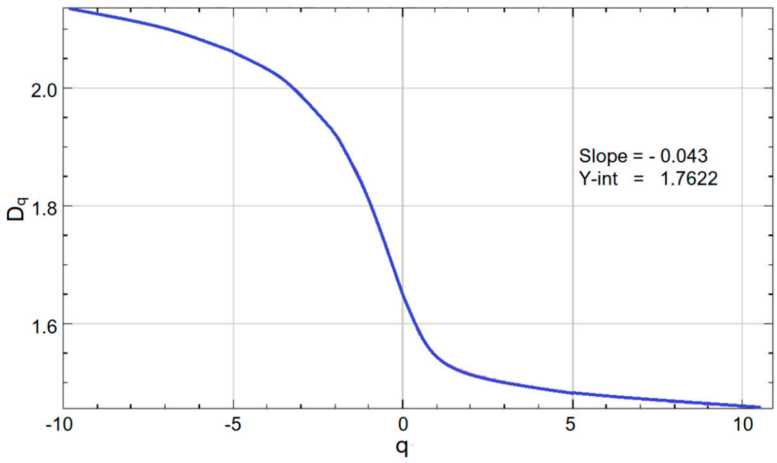

Figure 10. The generalized dimension, D_q, of the image from Figure 7b.

Figure 11 presents the $f(\alpha)$ –spectrum in one of the experiments for the corroded sample. The maximum value, max $f(\alpha) = 1.6534$, approximates the box dimension. The value in this experiment is in the range of the box dimension that was previously computed, [1.5257, 1.6689].

Another parameter used to characterize the multifractality in Fraclac software is the *aperture*, which is the slope of the segment joining the points A($q = 1$, $f(\alpha(q = 1))$) and B($q = -1$, $f(\alpha(q = -1))$). In these experiments, it varied between 0.2903 and 0.3567, with an average of 0.3213, corresponding to aperture lengths of 0.3692, 0.3943, and 0.3849, respectively.

Taking into account the values of the mass exponent, generalized dimensions, and $f(\alpha)$–spectrum and the shapes of their charts, it results that the corrosion pattern is multifractal.

Dlouhy' and Strnadel [38] showed that the rugosity of a corroded surface is determined by factors like the material structure and its mechanical characteristics. Additionally, microstructural heterogeneities are responsible for the material's resistance to crack initiation or propagation [60,61]. Corrosion produces a texture corresponding to the rough

structure of the surface. This surface is an indicator of corrosion intensity. Therefore, it is necessary to have an instrument for quantitatively estimating the surfaces of the objects after corrosion. The visual evaluation of the studied samples after the erosion–corrosion is important because the sample surface indicates the attack's intensity and morphology [47].

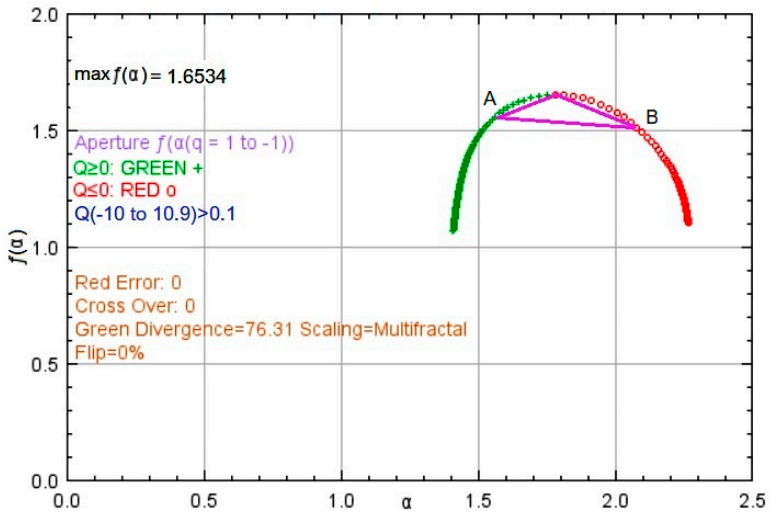

Figure 11. The $f(\alpha)$–spectrum of the image from Figure 7b.

The studies initiated by Mandelbrot [32] and continued by other scientists [60–66] confirmed the existence of a self-similarity pattern of the cracks propagation in different materials. Recent studies have indicated the same property of corroded materials [46–48].

Image characterization using fractal dimension based on micrographics is a very robust methodology, the texture of surface microstructural changes being independent of different variables like illumination. The advantage of the fractal approach to surface characterization is that it is insensitive to the structural details, and the structure is characterized by a single descriptor: the fractal dimension [38,67,68].

Different studies [32,62–65] have tried to determine the relationship between some steels' fracture toughness and the fracture's surface with no clear conclusions [38]. However, none analyzed the fractal behavior of the copper-based alloys in cavitation media. Therefore, the correlation between the surface's roughness, its fractal dimension after the corrosion, the copper alloy composition, and the crack propagation remains to be studied.

4. Conclusions

This article presents the fractal/multifractal analysis of a brass sample after the corrosion–erosion produced by cavitation. It was proved that the series of the mass loss values on the sample's surface has a box dimension near 1, in concordance with the equation of the deterministic linear model. Based on this result, a non-/monofractal behavior of the time series of the mass loss variation per sample's surface was expected. The chart of the mass exponent τ_q *vs.* q has a linear shape, whereas that of D_q vs. q is horizontal. Both indicate that the series does not present the multifractality property.

The results point out that the distribution of the corrosion damage on the material's surface is not uniform, being characterized by multifractality (highlighted by the multifractal spectrum). The computed box dimension of the SEM sample image was $d_{box} = 1.5692$, with a standard deviation of 0.0269. The S-shape of the generalized dimension and the existence of at least two regions with different shapes in the mass exponent chart of the same image show a clear multifractal behavior of the corroded sample. Moreover, the capacity, information, and correlation dimensions are, respectively, $d_{cap} = 1.5969$, $d_{inf} = 1.49836$ and $d_{cor} = 1.4670$.

The advantage of this study is that it can be performed for any material and liquid media. Additionally, experiments related to the mechanical properties of materials at

different erosion–corrosion stages should be performed to extract the correlation between the multifractal dimension of the corroded sample image and the sample's mechanical behavior. This study is only a first step in assessing the multifractal behavior of copper alloys in cavitation. The following aspects will be investigated in the future: (1) the variation of the fractal/multifractal behavior as a function of the samples' compositions, (2) the analysis of the fractal/multifractal behavior at different stages of the erosion –corrosion process before and after the first cracks apparition, and (3) the analysis of the fractal behavior of the cracks propagations in time. The study will be performed on different liquids and stationary or circulating media.

Author Contributions: Conceptualization, A.B.; methodology, A.B. and C.Ș.D.; software, A.B.; validation, A.B.; formal analysis, A.B. and C.Ș.D.; investigation, A.B. and C.Ș.D.; resources, A.B.; data curation, A.B. and C.Ș.D.; writing—original draft preparation, A.B.; writing—review and editing, C.Ș.D.; visualization, A.B.; supervision, A.B.; project administration, A.B.; funding acquisition, A.B. All authors have read and agreed to the published version of the manuscript.

Funding: This research received no external funding.

Institutional Review Board Statement: Not applicable.

Informed Consent Statement: Not applicable.

Data Availability Statement: Not applicable.

Conflicts of Interest: The authors declare no conflict of interest.

References

1. Flynn, H.G. Physics of acoustic cavitation in liquids. In *Physical Acoustics*; Mason, W.P., Ed.; Academic Press: New York, NY, USA, 1964; Volume 1, Part B, pp. 57–172.
2. Bai, L.; Yan, J.; Zeng, Z.; Ma, Y. Cavitation in thin liquid layer: A review. *Ultrason. Sonochem.* **2020**, *66*, 105092. [CrossRef] [PubMed]
3. Young, F.E. *Cavitation*; Mac Graw-Hill: Maidenhead, UK, 1989.
4. Rooney, J.A. *Ultrasound: Its Chemical, Physical and Biological Effects, Suslick*; VCH: New York, NY, USA, 1988.
5. Bărbulescu, A.; Dumitriu, C.Ș. Modeling the Voltage Produced by Ultrasound in Seawater by Stochastic and Artificial Intelligence Methods. *Sensors* **2022**, *22*, 1089. [CrossRef] [PubMed]
6. Dumitriu, C.S.; Dragomir, F.-L. Modeling the Signals Collected in Cavitation Field by Stochastic and Artificial Intelligence Methods. In Proceedings of the 2021 13th International Conference on Electronics, Computers and Artificial Intelligence (ECAI), Pitești, Romania, 1–3 July 2021; pp. 1–4. [CrossRef]
7. Schüssler, A.; Exner, H.E. The corrosion of nickel-aluminium bronzes in seawater—I. Protective layer formation and the passivation mechanism. *Corros. Sci.* **1993**, *3*, 1793–1802. [CrossRef]
8. Wharton, J.A.; Barik, R.C.; Kear, G.; Wood, R.J.K.; Stokes, K.R.; Walsh, F.C. The corrosion of nickel-aluminium bronze in seawater. *Corros. Sci.* **2005**, *47*, 3336–3367. [CrossRef]
9. Wharton, J.A.; Stokes, K.R. The influence of nickel–aluminium bronze microstructure and crevice solution on the initiation of crevice corrosion. *Electrochim. Acta* **2008**, *53*, 2463–2473. [CrossRef]
10. Basumatary, J.; Nie, M.; Wood, J.K. The synergistic effects of cavitation erosion-corrosion in ship propeller materials. *J. Bio-Tribo-Corros.* **2015**, *1*, 1–12. [CrossRef]
11. Basumatary, J.; Wood, R.J.K. Synergistic effects of cavitation erosion and corrosion for nickel aluminium bronze with oxide film in 3.5% NaCl solution. *Wear* **2017**, *376–377*, 1286–1297. [CrossRef]
12. Hamidah, I.; Solehudin, A.; Hamdani, A.; Hasanah, L.; Khairurrijal, K.; Kurniawan, T.; Mamat, R.; Maryanti, R.; Nandiyanto, A.B.D.; Belkheir, H. Corrosion of copper alloys in KOH, NaOH, NaCl, and HCl electrolyte solutions and its impact to the mechanical properties. *Alex. Eng. J.* **2021**, *60*, 2235–2243. [CrossRef]
13. Alfantazi, A.M.; Ahmed, T.M.; Tromans, D. Corrosion behavior of copper alloys in chloride media. *Mater. Des.* **2009**, *30*, 2425–2430. [CrossRef]
14. Bakhshandeh, H.R.; Allahkaram, S.R.; Zabihi, A.H. An investigation on cavitation-corrosion behavior of Ni/β-SiC nanocomposite coatings under ultrasonic field. *Ultrason. Sonochem.* **2019**, *56*, 229–239. [CrossRef]
15. Dumitriu, C.S.; Bărbulescu, A. *Studies on the Copper Based Alloys Used in Naval Constructions-Modeling the Mass Loss in Different Media*; Sitech: Craiova, Romania, 2007. (In Romanian)
16. Peng, S.; Xu, J.; Li, Z.; Jiang, S.; Xie, Z.-H.; Munroe, P. Electrochemical noise analysis of cavitation erosion corrosion resistance of NbC nanocrystalline coating in a 3.5 wt% NaCl solution. *Surf. Coat. Tech.* **2021**, *415*, 127133. [CrossRef]
17. Ivanov, I.V. *Corrosion Resistant Materials in Food Industry*; Editura Agro-Silvica: Bucharest, Romania, 1959. (In Romanian)

18. Dumitriu, C.S. On the corrosion of two types of bronzes under cavitation. *Ann. Dunarea Jos Univ. Galati Fascicle IX Metall. Mater. Sci.* **2021**, *4*, 12–16. [CrossRef]
19. Dumitriu, C.S.; Bărbulescu, A. Copper corrosion in ultrasound cavitation field. *Ann. Dunarea Jos Univ. Galati Fascicle IX Metall. Mater. Sci.* **2021**, *3*, 31–35. [CrossRef]
20. Fortes-Patella, R.; Choffat, T.; Reboud, J.L.; Archer, A. Mass loss simulation in cavitation erosion: Fatigue criterion approach. *Wear* **2013**, *300*, 205–215. [CrossRef]
21. Mandelbrot, B.B. *Fractals, Form, Chance and Dimension*; W. H. Freeman & Co. Ltd.: San Francisco, CA, USA, 1977.
22. Bărbulescu, A.; Șerban, C. Statistical and multifractal analysis of rainfall of Romania. *Int. J. Ecol. Econ. Stat.* **2012**, *25*, 1–11.
23. Burlando, P.; Menduni, G.; Rosso, R. (Eds.) Fractals, scaling and nonlinear variability in hydrology. *J. Hydrol.* **1996**, *187*, 1–264.
24. Chen, G.; Cheng, Q. Fractal density modeling of crustal heterogeneity from the KTB deep hole. *J. Geophys. Res. Solid Earth* **2017**, *122*, 1919–1933. [CrossRef]
25. Bărbulescu, A.; Dumitriu, C.S. Assessing the Fractal Characteristics of Signals in Ultrasound Cavitation. In Proceedings of the 25th International Conference on System Theory, Control and Computing, Iasi, Romania, 20–23 October 2021; ICSTCC 2021. [CrossRef]
26. Sun, W.; Xu, G.; Gong, P.; Liang, S. Fractal analysis of remotely sensed images: A review of methods and applications. *Int. J. Remote Sens.* **2006**, *27*, 4963–4990. [CrossRef]
27. Nichita, M.-V.; Paun, M.-A.; Paun, V.-A.; Paun, V.-P. Pulmonary X-ray Images. A Fractal Analysis. *AIP Conf. Proc.* **2020**, *2218*, 050003. [CrossRef]
28. Tanabe, N.; Sato, S.; Suki, B.; Hirai, T. Fractal Analysis of Lung Structure in Chronic Obstructive Pulmonary Disease. *Front. Physiol.* **2020**, *11*, 603197. [CrossRef]
29. Updike, S.X.; Nowzari, H. Fractal analysis of dental radiographs to detect periodontitis-induced trabecular changes. *J. Periodont. Res.* **2008**, *43*, 658–664. [CrossRef]
30. Kato, C.N.A.O.; Barra, S.G.; Tavares, N.P.K.; Amaral, T.M.P.; Brasileiro, C.B.; Mesquita, R.A.; Abreu, L.G. Use of fractal analysis in dental images: A systematic review. *Dentomaxillofac. Radiol.* **2020**, *49*, 20180457. [CrossRef]
31. Parkinson, I.H.; Fazzalari, N.L. Methodological principles for fractal analysis of trabecular bone. *J. Microsc.* **2000**, *198*, 138–142. [CrossRef]
32. Mandelbrot, B.B.; Passoja, D.E.; Paullay, A.J. Fractal character of fracture surfaces of metals. *Nature* **1984**, *308*, 721–722. [CrossRef]
33. Shi, D.W.; Jiang, J.; Lung, C.W. Correlation between the scale-dependent fractal dimension of fracture surfaces and the fracture toughness. *Phys. Rev. B Condens. Matter.* **1996**, *54*, R17355–R17358. [CrossRef]
34. Zhang, H.; Wei, D.-M. Estimation of fracture toughness, driving force, and fracture energy for fractal cracks using the method of imaginary smooth crack. *Eng. Fract. Mech.* **2010**, *77*, 621–630. [CrossRef]
35. Borodich, F.M. Fractals and fractal scaling in fracture mechanics. *Int. J. Fract.* **1999**, *95*, 239–259. [CrossRef]
36. Ji, H.; Jiang, H.; Zhao, R.; Tian, Y.; Jin, X.; Jin, N.; Tong, J. Fractal Characteristics of Corrosion-Induced Cracks in Reinforced Concrete. *Materials* **2020**, *13*, 3715. [CrossRef]
37. Zavdoveev, A.; Beygelzimer, Y.; Varyukhin, V.; Efros, B. Influence of Deformation on Fractal Dimension of Deformed Metals Structure. Available online: https://www.researchgate.net/publication/224871709_Influence_Of_Deformation_On_Fractal_Dimension_Of_Deformed_MetalsStructure (accessed on 19 August 2022).
38. Dlouhý, I.; Strnadel, B. The effect of crack propagation mechanism on the fractal dimension of fracture surfaces in steel. *Eng. Fracture Mech.* **2008**, *75*, 726–738. [CrossRef]
39. Li, W.; Wu, M.; Shi, T.; Yang, P.; Pan, Z.; Liu, W.; Liu, J.; Yang, X. Experimental Investigation of the Relationship between Surface Crack of Concrete Cover and Corrosion Degree of Steel Bar Using Fractal Theory. *Fractal Fract.* **2022**, *6*, 325. [CrossRef]
40. Xu, Y.; Qian, C.; Pan, L.; Wang, B.; Lou, C. Comparing Monofractal and Multifractal Analysis of Corrosion Damage Evolution in Reinforcing Bars. *PLoS ONE* **2012**, *7*, e29956. [CrossRef]
41. Davies, S.; Hall, P.J.R. Fractal analysis of surface roughness by using spatial data. *Statist. Soc. B* **1999**, *61*, 3–37. [CrossRef]
42. Karolczak, P.; Kowalski, M.; Raszka, K. The application of fractal analysis to the description of brushed steel surfaces. *J. Mach. Eng.* **2020**, *20*, 99–115. [CrossRef]
43. Kim, J.J.; Hwang, W.S. Evaluation of a fractal analysis technique for corrosion studies. *Met. Mater. Int.* **2012**, *18*, 783–789. [CrossRef]
44. Songbo, R.; Song, G.; Chao, K.; Shenghui, Z.; Ying, G.; Gang, L.; Tao, Y.; Liqiong, Y. Fractal characteristic of corroded steel surface and application to the fracture analyses. *Constr. Build. Mater.* **2022**, *340*, 127759. [CrossRef]
45. Zhang, H.; Xu, S.; Zhang, Z.; Nie, B.; Wang, L. Fracture analysis of corroded cold-formed thin steel plates based on actual morphology using micromechanical models. *Constr. Build. Mater.* **2021**, *267*, 120899. [CrossRef]
46. Sarmiento, E.; Gonzalez-Rodriquez, J.G.; Urichurtu, J. Fractal Analysis of the Corrosion Inhibition of Carbon Steel in a Bromide Solution by Molybdates. *ECS Trans.* **2008**, *15*, 221. [CrossRef]
47. García-Ochoa, E.; Corvo, F. Copper patina corrosion evaluation by means of fractal geometry using electrochemical noise (EN) and image analysis. *Electrochem. Commun.* **2010**, *12*, 826–830. [CrossRef]
48. López, J.L.; Veleva, L. 2D-DFA as a tool for non-destructive characterisation of copper surface exposed to substitute ocean water. *Phys. A Stat. Mech. Appl.* **2022**, *586*, 126490. [CrossRef]

49. Dumitriu, C.S.; Bărbulescu, A. Artificial intelligence models for the mass loss of copper-based alloys under the cavitation. *Materials* **2022**, *15*, 6695. [CrossRef]
50. Jin, F.; Chiang, F.P. Nondestructive Evaluation of Corrosion by Fractal Geometry. *Res. Nondestruct. Eval.* **1996**, *7*, 229–238. [CrossRef]
51. Vuidel, G.; Tannier, C. Fractalyse 3.0. User Manual. Available online: https://sourcesup.renater.fr/www/fractalyse/download/manual-en.pdf (accessed on 23 August 2022).
52. Weisstein, E.W. Capacity Dimension. Available online: https://mathworld.wolfram.com/CapacityDimension.html (accessed on 23 August 2022).
53. Baker, G.L.; Gollub, J.B. *Chaotic Dynamics: An Introduction*, 2nd ed.; Cambridge University Press: Cambridge, UK, 1996.
54. Falconer, K. *Fractal Geometry: Mathematical Foundations and Applications*, 3rd ed.; John Wiley & Sons, Ltd.: Chichester, UK, 2014.
55. Halsey, T.; Jensen, M.; Kadanoff, L.; Procaccia, I.; Shraiman, B.I. Fractal measures and their singularities: The characterization of strange sets. *Phys. Rev. A* **1986**, *33*, 1141–1151. [CrossRef] [PubMed]
56. Ferraris, L.; Gabellani, S.; Parodi, U.; Rebora, N. Revisiting Multifractality in Rainfall Fields. *J. Hydrometeorol.* **2003**, *4*, 544–551. [CrossRef]
57. Stanley, H.E.; Meakin, P. Multifractal phenomena in physics and chemistry. *Nature* **1998**, *335*, 405–409. [CrossRef]
58. Hentschel, H.G.E.; Procaccia, I. The infinite number of generalized dimensions of fractals and strange attractors. *Phys. D Nonlinear Phenom.* **1983**, *8*, 435–444. [CrossRef]
59. Fraclac for ImageJ. Available online: https://imagej.nih.gov/ij/plugins/fraclac/FLHelp/Introduction.htm (accessed on 23 November 2022).
60. Bouchaud, E. Scaling properties of cracks. *J. Phys. Condens. Mater.* **1997**, *9*, 4319–4344. [CrossRef]
61. Bouchaud, E.; Bouchaud, J.P.; Fisher, D.S.; Ramanathan, S.; Rice, J.R. Can crack front waves explain the roughness of cracks? *J. Mech. Phys. Solids* **2002**, *50*, 1703–1725. [CrossRef]
62. Dauskart, R.H.; Haubensak, F.; Ritchie, R.O. On the interpretation of the fractal character of fracture surfaces. *Acta Metall.* **1990**, *38*, 143–159. [CrossRef]
63. Gokhale, A.M.; Underwood, E.E. A general method for estimation of fracture surface roughness: Part I. Theoretical aspects. *Metall. Trans. A* **1990**, *21*, 1193–1199. [CrossRef]
64. Huang, Z.H.; Tian, J.F.; Wang, Z.G. A study of the slit island analysis as a method for measuring fractal dimension of fractured surface. *Scripta Metall. Mater.* **1990**, *24*, 967–972. [CrossRef]
65. Imre, A.; Paykossy, T.; Nyikos, L. Electrochemical determination of the fractal dimension of fractured surfaces. *Acta Metall. Mater.* **1992**, *40*, 1819. [CrossRef]
66. Jiang, X.G.; Chu, W.Y.; Hisao, C.M. Relationship between JIC and fractal value of fracture surface of ductile materials. *Acta Metall. Mater.* **1994**, *42*, 105–108. [CrossRef]
67. Quevedo, R.; Lopez-G, C.; Aguilera, J.M.; Cadoche, L. Description of Food Surfaces and Microstructural Changes Using Fractal Image Texture Analysis. *J. Food Eng.* **2002**, *53*, 361–371. [CrossRef]
68. Risovic, D.; Mahovic, S.; Poljacek, K.; Furic, M.; Gojo, M. Inferring fractal dimension of rough/porous surfaces—A comparison of SEM image analysis and electrochemical impedance spectroscopy methods. *Appl. Surf. Sci.* **2008**, *255*, 3063–3070. [CrossRef]